Numerical Study of the Aerodynamic Interference of Rotors Imposed on Fuselage for a Quadcopter

YIFEI ZHU[iD], DEFU LIN[iD], LI MO, PEIJIAN LV[iD], AND JIANCHUAN YE[iD]
School of Aerospace Engineering, Beijing Institute of Technology, Beijing 100081, China
Beijing Key Laboratory of UAV Autonomous Control, Beijing Institute of Technology, Beijing 100081, China

Corresponding author: Peijian Lv (lexluck88@163.com)

ABSTRACT This paper investigates the transient aerodynamic interference of rotors imposed on fuselage for a quadcopter through Computational Fluid Dynamics (CFD) simulations. The numerical study of transient effects due to rotor rotation is enabled by sliding mesh which defines the rotation domains encompassing rotor blades. The results show that the interference effects of rotor change the aerodynamic forces of the fuselage, causing about 67% in-crease in lift, 13% increase in drag, and 90% increase in pitching up moment on average. The variations of fuselage lift are associated with the pressure distribution changes due to rotors rotation, the high-pressure areas and low-pressure areas over the rotor projects on the arms of the quadcopter causing periodical abrupt changes on the lift, drag and pitching moment.

INDEX TERMS Numerical simulation.

I. INTRODUCTION

Quadcopters have increasingly been used in a large variety of applications, such as military [1]–[3], rescue [4]–[6], photography, agriculture, prospecting, logistics [7], etc. Most scenarios demand high performance in flight speed, range, and/or endurance. Due to the rotation of multiple lifting surfaces, the aerodynamics of quadcopters are highly interactive and time-dependent. The unsteady aerodynamic characteristic changes the performance of quadcopter. Therefore, it is essential to study the aerodynamic interference caused by the rotors of quadcopters.

Previous research studied the aerodynamics of quadcopters through numerical simulations. Hwang *et al.* [8] studied the mutual aerodynamic interference between the rotors and the fuselage through unsteady-flow RANS simulation with overset-mesh technique, mainly focusing on the interference between rotors. Compared with an independent rotor, Barcelos *et al.* [9] investigates the aerodynamic differences between a diamond and a square configurations on a quadcopter by employing potential flow method, so that aerodynamic interference between rotors is investigated. Luo *et al.* [10] proposed a mathematical model by involving rotor wake interference, so that a quadcopter in forward flight can be modeled as a circular fixed wing with

Glauert's high-speed approximation [11], transient numerical simulation is performed to access the aerodynamics of rotors. Fu *et al.* [12] performed numerical study of a rotor to evaluate the aerodynamic characteristics of the slipstream through RANS simulations with structured patched grids and sliding mesh. Misiorowaski *et al.* [13] performs detached-eddy simulation with a simplified model represented by four rotors. Sectional forces over each rotor disc are accessed in this study, so that the pattern of change in aerodynamic force due to interference among rotors is elaborated.

These previous studies show that the aerodynamics interference leads to periodical changing forces acting on the four rotors, and this should be considered in control algorithm to improve the performance of quadcopter [14]. On the other side, aerodynamic interference also causes periodical variation of the force imposed on the fuselage. Attempts were made to access this interference effect, and the periodical changing forces are expressed with the time-averaged values [8], [11], [13]. However, to our best knowledge, very few studies try to address the aspect of time-dependent characteristic of this interference imposed on the fuselage [10], [15]. This, together with the lack of insight of flow mechanisms, inspired the presented work to investigate the transient aerodynamics between the rotors and fuselage.

The presented work tries to contribute to the understanding of flow mechanisms associated with periodical variations of aerodynamic forces imposed on the fuselage.

The associate editor coordinating the review of this manuscript and approving it for publication was Dipankar Deb[iD].

Time-dependent laws for this transient aerodynamic interference are analyzed, so that the correlation between the transient interference on fuselage and the rotation of rotors blades is established. To enable the investigation of transient aerodynamics, two technics, namely frequency-domain analysis and time-domain analysis are employed.

In this study, aerodynamic interference is evaluated as the difference between a quadcopter and its fuselage without rotors. The flight condition is kept in a constant speed, and the fuselage and rotor blades are assumed rigid. This numerical study employs unsteady incompressible Reynolds-Averaged Navier-Stokes (RANS) simulations. Computational domain consists of rotation domains to address the periodical rotating motion of rotors [10], [13], [16], [17]. The proposed simulations enable the quantification of transient aerodynamic interference effects.

In this paper, section II introduces the methods employed in this study. The approach of evaluating aerodynamic interference and the geometric models of a quadcopter is elaborated. The conditions of numerical simulations and computational domain are introduced. Section III discusses the simulation results. The periodical variations of lift, drag and pitching moment of the fuselage is quantified. Flow mechanisms associated with the aerodynamic inference are analyzed. Section IV presents the conclusions and future works of this research.

II. SIMULATION METHODS AND PROCEDURES

A. QUANTIFICATION OF AERODYNAMIC INTERFERENCE

This study evaluates the aerodynamic interference as the change of aerodynamic forces (and moments) due to rotor rotation. For this purpose, two configurations are defined: quadcopter and isolated fuselage, as shown in Fig. 1. The isolated fuselage (Fig. 1b) is extracted from the quadcopter (Fig. 1a) by removing rotors. The change of aerodynamic forces is quantified as the difference between the forces of the isolated fuselage and that of the quadcopter, as given in (1-3). ΔC_L, ΔC_D and ΔC_M denote the change in the coefficients of lift, drag and pitching moment, respectively. The subscripts of UAV and fuselage correspond to the configurations of quadcopter and isolated fuselage illustrated in Fig. 1. The isolated fuselage is further decomposed into a body and arms, as shown in Fig. 1c and Fig. 1d. All of these components are assumed to be rigid. This decomposition enables the investigation of aerodynamic interference effects imposed on these components.

$$\Delta C_L = C_{L,\text{UAV}} - C_{L,\text{fuselage}} \quad (1)$$

$$\Delta C_D = C_{D,\text{UAV}} - C_{D,\text{fuselage}} \quad (2)$$

$$\Delta C_M = C_{M,\text{UAV}} - C_{M,\text{fuselage}} \quad (3)$$

B. MODEL GEOMETRY

This study employs a simplified model to represent a typical quadcopter, consisting of a fuselage, four arms and four rotors, while motors and landing gears are ignored. The
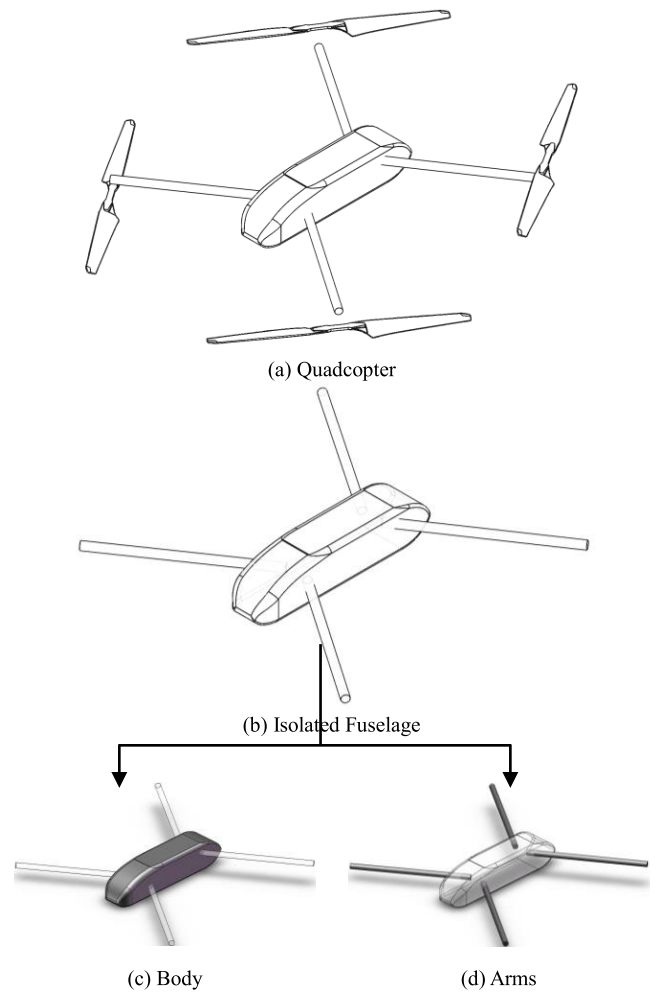

(a) Quadcopter

(b) Isolated Fuselage

(c) Body   (d) Arms

FIGURE 1. Configurations of quadcopter and isolated fuselage.

dimensions of the model are illustrated in Fig 1. This study employs four 20.4 × 9 T-MOTOR MF2009 rotors. R denotes the rotor radius of 259mm. d (1.21R, 314mm) corresponds to the projection distance between the center of a rotor and the symmetry plane (x-z plane), while y_0 (0.17R, 45mm) is the half width of the fuselage. The simplified geometry body represents a typical body of quadcopter. It is noted that front arms are mounted slightly higher than the rear arms, this enables easy folding of the arms for packaging.

The identification and rotational direction of four rotors refers to the notation of Barcelos [9]: the front rotors are in the inward-out direction, while the direction of rear rotors are opposite. φ stands for the azimuth angle of rotors. The initial azimuth angle (at t = 0s) for front and rear rotors are randomly set at 55 degrees ($\varphi_{f0} = 55°$, $\varphi_{r0} = 55°$), as shown in Fig.2c) Aerodynamic force of lift and drag correspond to the wind coordinates ($O_{\text{w}}x_{\text{w}}y_{\text{w}}z_{\text{w}}$), obtained by rotating the body-fixed coordinate system ($O_{\text{b}}x_{\text{b}}y_{\text{b}}z_{\text{b}}$, in Fig.2d) by the angle of attack α around the y-axis. In the wind coordinates system, the positive value of M_y denotes the nose-up momentum. It is noted that the lift of the isolated fuselage L_f is negative under forward flight condition, which should
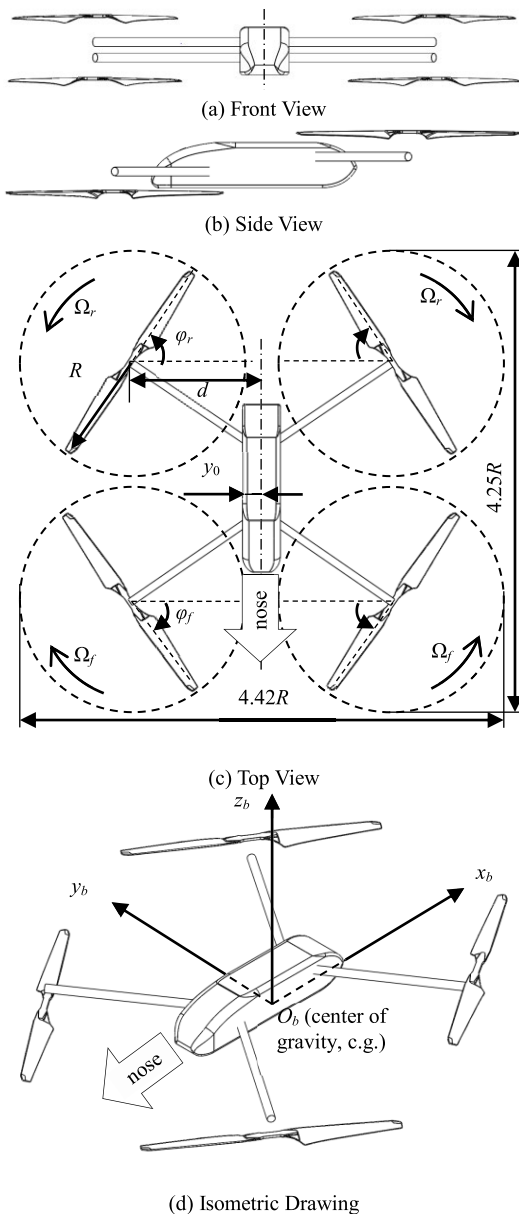
(a) Front View

(b) Side View

(c) Top View

(d) Isometric Drawing

FIGURE 2. Dimensions of the quadcopter model.

TABLE 1. Flight condition.

V_∞(m/s)	α(deg)	Ω_f(r/min)	$2f_f$(Hz)	Ω_r(r/min)	$2f_r$(Hz)
15	8	3129	104.30	3323	110.77

TABLE 2. Material properties.

ρ (kg/m³)	C_P (J/kg·K)	Thermal Conductivity (W/m·K)	Viscosity (kg/m·s)
1.225	1006.43	0.0242	1.7894e-05

TABLE 3. Reference parameters.

Re (Reynolds Number)	S (Reference Area, m²)	l (Reference Length, m)
398429	0.025	0.388

D. COMPUTATIONAL DOMAIN AND MESH SENSITIVITY ANALUSIS

This numerical study employs transient incompressible RANS simulations by using commercial software Fluent [10], [16]. The rotation of rotors is enabled by sliding mesh method. One single time step of the transient simulation is set as 0.0001s to obtain the angular resolution of about 1.88 degrees for front rotors. To address viscous flow, this simulation adopts Realizable k-ε turbulence model with standard wall functions [10]. In terms of the solution methods,

be balanced by the component of rotors' thrust due to the negative angle of attack of the quadcopter.

C. SIMULATION CONDITION

The simulation of quadcopter is kept in the forward flight condition with a constant wind speed of 15m/s. TABLE 1 lists relevant parameters for this flight condition according to a flight test. It is noted that the rotational speed of two rear rotors is slightly higher than that of front ones, so that a nose-down moment is generated to maintain the nose-down attitude for level flight. TABLE 2 provides air properties in the simulations. Reynolds number and reference values for no dimensioning of aerodynamic forces are given in TABLE 3.

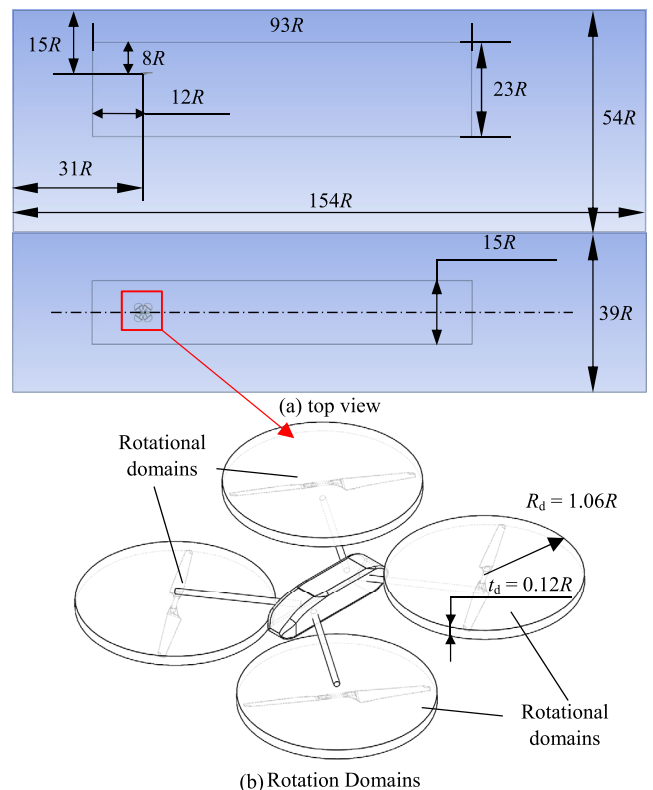

(a) top view

(b) Rotation Domains

FIGURE 3. Scheme of computational domain.

second order upwind method is chosen for the pressure-based solver. SIMPLE method is employed to deal with the pressure-velocity coupling.

This simulation assumes rigid fuselage and rotor blades [13], [19]. Computation domain is rectangular shaped with dimensions of $154R \times 39R \times 54R$ (20m × 5m × 7m), as shown in Fig. 3a. The ratio of the quadcopter cross-section area over the domain cross-section area is less than 0.2%, keeping a negligible blockage effect. Four cylindrical rotation domains encompassing rotor blades are $1.06R$ (550mm) in diameter, $0.12R$ (30mm) in thickness with a 0 degrees incident angle (the angle between the rotor disc and x-y plane), as shown in Fig. 3c.

The domain is discretized into unstructured tetrahedron cells and prism cells, as shown in Fig. 4. Mesh is refined in the vicinity of the quadcopter as well as in the downstream region, as illustrated in Fig. 3b. Prism mesh [18] is distributed over the wall boundary of the fuselage and rotors to deal with boundary layer flow Fig. 3c). There are total 10 layers of prism cells with 10% growth rate, as shown in Fig. 3c. The height of the first layer of prism cells is set as 0.0001m, keeping the y+ value less than 5 for the prescribed simulation conditions. To deal with rotational domains, the interface boundary between rotational domains and the fixed domain ensures data transmitting.

A mesh sensitive analysis is performed for the isolated fuselage to determine a proper cell number for simulations. The simulation condition in this analysis is kept the same as in the actual numerical simulations. TABLE 4 describes 9 test cases with different mesh cell quantities. Fig. 5 shows the variation of drag coefficient $\Delta C_{D,\text{fuselage}}$ for 9 tested cases
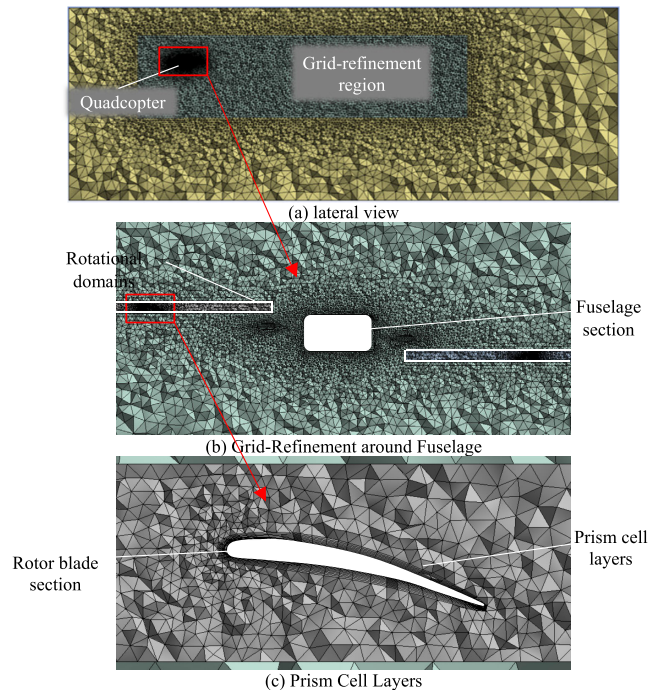
with different mesh cell quantities. It is noted that the drag coefficient of the densest mesh (23.39 million) is set as a reference to evaluate $\Delta C_{D,\text{fuselage}}$ in this analysis. The case of 3.55 million tetrahedrons mesh is within the asymptotic range and exhibits a balance between. accuracy and efficiency. As a result, it is adopted for the following simulations.

TABLE 4. Test cases with different mesh cell quantities.

Mesh cell quantities (Million)	Cell size of fuse-lage body surface (m)	Cell size of grid-refinement do-main (m)	Cell size of far field (m)
0.78	0.008	0.4	1.0
3.10	0.004	0.1	0.5
3.55	0.0035	0.1	0.5
5.10	0.003	0.08	0.3
6.00	0.0025	0.08	0.3
7.46	0.002	0.08	0.3
9.40	0.0015	0.1	0.5
16.70	0.001	0.1	0.5
23.39	0.0008	0.1	0.5

III. RESULTS AND DISCUSSION

This section elaborates the results of numerical simulations. Nondimensional forces (and moment) of the fuselage for the two configurations (quadcopter and isolated fuselage) are plotted in Fig. 6 where the azimuth angle of front rotors is set as the x-axis. This plot shows the variation of aerodynamic forces in one revolution (360 degrees of front rotor). It is noted that values for the isolated fuselage keep constant. These plots visualize the aerodynamic interference due to rotor rotation as the variations of aerodynamic forces (and moment).

TABLE 5 lists the mean values of aerodynamic forces and moment for two configurations. The differences between these parameters are positive, denoting that the rotor rotation leads to the tendency of lifting up, deceleration, and nose up. On average, the aerodynamic interference due to rotor ration
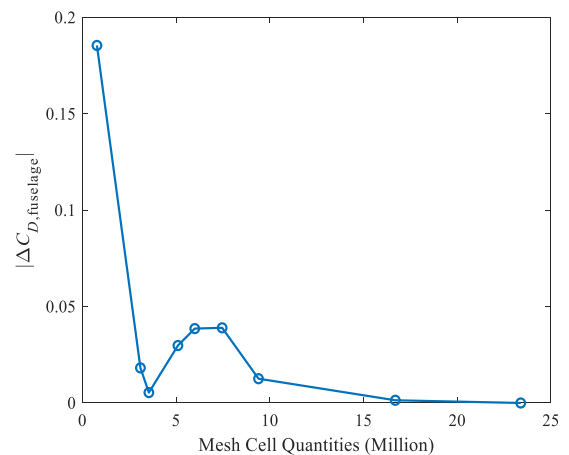

FIGURE 4. Mesh distribution.

FIGURE 5. Mesh sensitivity analysis (change of $\Delta C_{D,\text{fuselage}}$ vs mesh cell quantities).
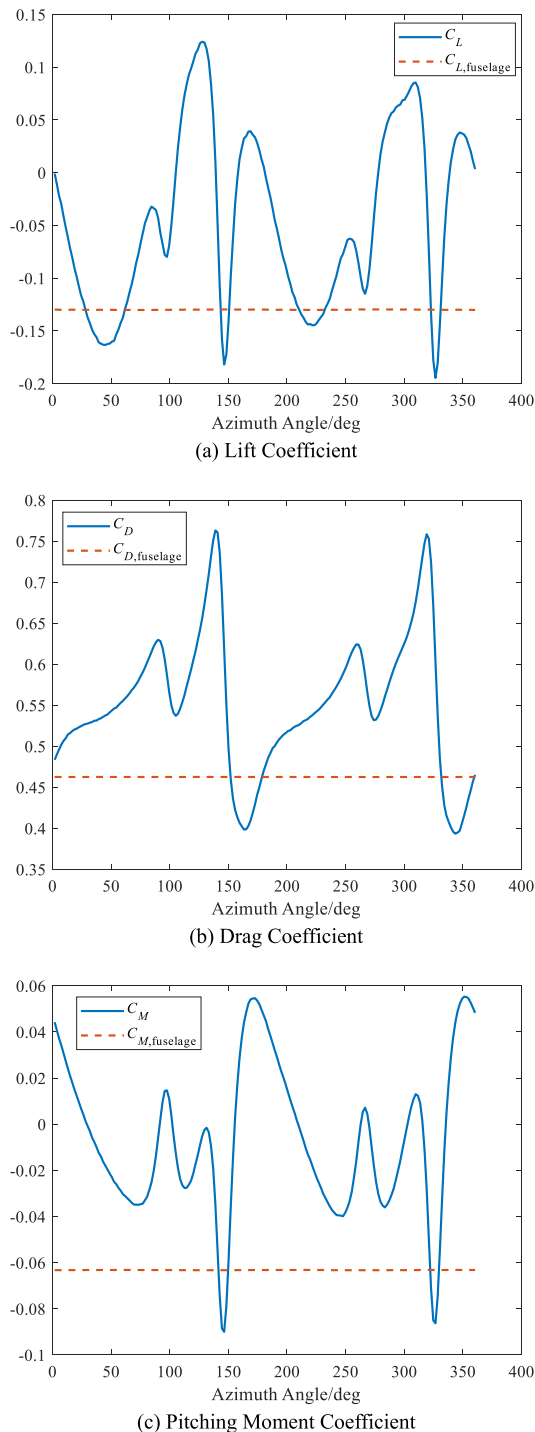
FIGURE 6. Correlation between nondimensional force/moment and the azimuth angle of front rotors (quadcopter and isolated fuselage).

accounts for about 67% additional lift, 13% additional drag and 90% pitching up moment. Moreover, it is necessary to study the transient impact that how rotors periodically change the aerodynamic forces imposed on the fuselage.

A. VARIATION IN LIFT COEFFICIENT

Lift is the key aerodynamic force to be considered in the discussion aerodynamic interference. Fast Fourier

TABLE 5. Mean value of aerodynamic forces and moments.

	C_L	C_D	C_M
UAV	-0.0430	0.5522	-0.0066
Fuselage	-0.1299	0.4625	-0.0632
Δ	0.0869	0.0897	0.0566
Difference ($\left\|\frac{\Delta \times 100\%}{\text{Fuselage}}\right\|$)	66.90%	13.39%	89.56%

Transform (FFT) analysis is performed to decompose the aerodynamic interference of ΔC_L in frequency domain. The results plotted in Fig. 7 covers interested frequencies ranging from 0 to 900Hz. It is noted that the peaks of frequency appear in pairs pattern, and these peaks could be related to the multiples of the frequency due to rotor rotation. The peaks in the first pair (1X) are marked as A and B in Fig. 7. Point A corresponds to the frequency of the front rotor rotation $2f_f$, while Point B refers to that of the rear rotor $2f_r$. TABLE 6 show that the difference between the peak frequency obtained through FFT analysis ($2f'_f$) and frequency of the rotors rotation $2f_f$ is less than 0.5% for the front rotors. Similarly, TABLE 7 shows the difference is negligible for the rear rotors. This FFT analysis also show that the amplitudes of peaks for the front rotors are higher than that of the rear rotor, this phenomenon is analyzed in following discussion. In short, FFT analysis suggest a strong connection between the lift change ΔC_L and the frequency of rotor rotation.

Time domain analysis is performed to study the aerodynamic interference of ΔC_L. Due to the constant rotational speed, the variable of time is expressed as the azimuth angle of the front rotor in this analysis. The variation of ΔC_L is presented in Fig. 8 (one revolution for about 0.019s). It is noted that the value of ΔC_L keeps positive in the most part of the cycle in Fig. 8, corresponding to the 66.9% increase of lift on average. This increase might be associated with the upwash due to the blade tip vortices. Fig. 9 shows the vectors of tangential velocity and contours of pressure coefficient (C_P) with vorticity in on a survey plane perpendicular to the free stream. This figure highlights a pair of tip vortices generated by the front rotors beneath the arms. The left vortex rotates counterclockwise, and the right one rotates clockwise, causing upwash flow lifting the fuselage.

In order to study the variation of lift due to rotor rotation, the lift (coefficient) of fuselage C_L is further broken down, as shown in Fig. 10. Five interest points are marked with triangles in this plot for following discussion of flow mechanisms associated with the sine-like periodical variation of ΔC_L. The curve for $C_{L,\text{Body}}$ represents the coefficient of lift imposed on the component of a single body, and the $C_{L,\text{Arm}}$ curve denotes the coefficient of lift force of four arms. It is noted that $C_{L,\text{fuselage}}$ is a constant (-0.1299) as listed in Table 5. As a result, the variations of ΔC_L, $\Delta C_{L,\text{Body}}$ and $\Delta C_{L,\text{Arm}}$ are equivalent to that of C_L, $C_{L,\text{Body}}$ and $C_{L,\text{Arm}}$. This equivalence of variation in aerodynamic force coefficient is the same in Figure 15, 19 and 20 in following paragraphs.
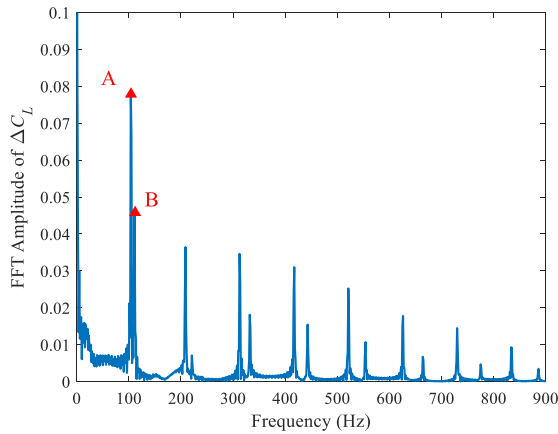
FIGURE 7. Results of FFT analysis: frequencies vs. amplitudes of ΔC_L (A corresponds to $2f_f = 104.3$Hz, B corresponds to $2f_f = 110.7$Hz).

TABLE 6. Comparison of front rotor frequencies.

	The Multiple of Frequency						
	1x	2x	3x	4x	5x	6x	7x
$2f_f$ (Hz)	104.3	208.6	312.9	417.2	521.5	625.8	730.1
	0	0	0	0	0	0	0
$2f_f'$ (Hz)	103.8	208.7	312.5	417.5	521.2	626.2	730.0
	0	0	0	0	0	0	0
Error	0.48%	0.05%	0.13%	0.07%	0.06%	0.06%	0.01%

TABLE 7. Comparison of rear rotor frequencies.

	The Multiple of Frequency						
	1x	2x	3x	4x	5x	6x	7x
$2f_f$ (Hz)	110.7	221.5	332.3	443.0	553.8	664.6	775.3
	7	4	1	8	5	2	9
$2f_f'$ (Hz)	111.1	220.9	332.0	443.1	554.2	664.1	775.1
	0	0	0	0	0	0	0
Error	0.30%	0.29%	0.09%	0.00%	0.06%	0.08%	0.04%

Figure 10 shows that $C_{L,\text{Body}}$ curve exhibits sine-like variations with a period of about 180°. On the other side, $C_{L,\text{Arm}}$ curve shows a more complex serpentine pattern which is elaborated in following paragraphs. This decomposition shows that the variation of $\Delta C_{L,\text{Body}}$ is mainly responsible for 180° period sine-like variation of ΔC_L.

The cause of variation of lift of body $C_{L,\text{Body}}$ can be analyzed through the change of pressure ΔC_P over the body surface. ΔC_P is defined in (4), as the difference between the pressure coefficients of quadcopter and that of the isolated fuselage. The subscripts of UAV and fuselage represent quadcopter and isolated fuselage in (4). Contours of ΔC_P are illustrated by Fig. 11. The range of ΔC_P is symmetrically set from −0.15 to 0.15, with cold color for negative value and warm color for positive value. This plot presents three cases corresponding to φ_f at Point E ($\varphi_f = 43°$), F ($\varphi_f = 139°$) and G ($\varphi_f = 222°$). These cases intuitively explain the variation of $C_{L,\text{Body}}$: In the E-F interval, pressure on the top-body significantly decreases as marked in the red circle,
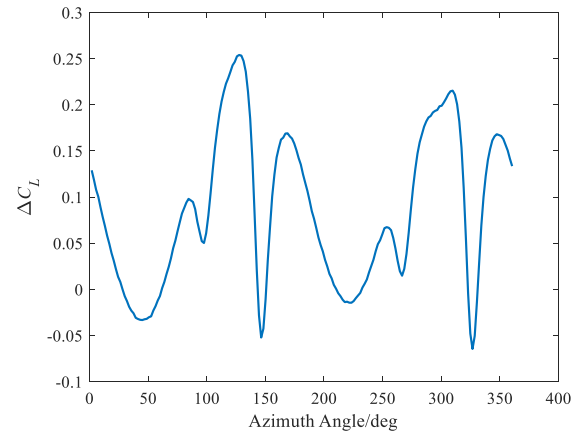

FIGURE 8. Correlation between ΔC_L and front rotors azimuth angle.

while pressure on the bottom-body mildly increases. The pressure distribution at Point G is similar to that at Point E The pressure change on the top-body and bottom-body contributes to the variation of lift, coincide with the variation of $C_{L,\text{Body}}$ plotted in Fig. 10. It should be clear that the pressure change on the left and right sides of body doesn't change lift, because the corresponding surface is parallel to the direction of lift. In short, this analysis shows that $\Delta C_{L,\text{Body}}$ changes in a sine-like law with φ_f is mainly contributed by the negative ΔC_P area on the top-body surface.

$$\Delta C_P = C_{P,\text{UAV}} - C_{P,\text{fuselage}} \quad (4)$$

To investigate the mechanism for the pressure distribution changes, the ΔC_P contours for the A-A plane from Point E to G are depicted, as shown in Fig. 11. Contours at Point E and G are similar, corresponding to similar values at Point E and G in Fig. 10. The top-body is immersed in low pressure which produced by the upper surface of the front rotors, causing additional lift. That's why $C_{L,\text{Body}}$ reaches the peak at Point F. Moreover, at Point E and G, the low-pressure from the upper surface of front rotors has lean effect to the body, leading to the troughs in Fig. 10. Therefore, the periodical variation of $C_{L,\text{Body}}$ is caused by the low-pressure over the upper surface of the front rotors when rotor rotates.

The lift imposed on the arms $C_{L,\text{Arm}}$ exhibits a more complex pattern of variation. The change of $C_{L,\text{Arm}}$ coincides with that of $C_{L,\text{Body}}$ at the Point E and G, as shown in Fig. 13. It implies that the same flow mechanism of lift variation of arms. Moreover, point C ($\varphi_f = 98°$) and D ($\varphi_f = 146°$) are heighted as two troughs in the variation of $C_{L,\text{Arm}}$, suggesting different flow mechanisms. To investigate the flow physics associated with the trough at Point C, three cases at φ_f values of 84°, 98° (Point C) and 128° are examined. Pressure distribution around the rear arms is presented as contours of C_P at a cutting plane B-B in Fig. 13. It is noted the rear rotors turn to the parallel position above the rear arms at Point C, the pressure over the top surface of rear arms is increased, due to the projection of the high pressure of the rotor blade.
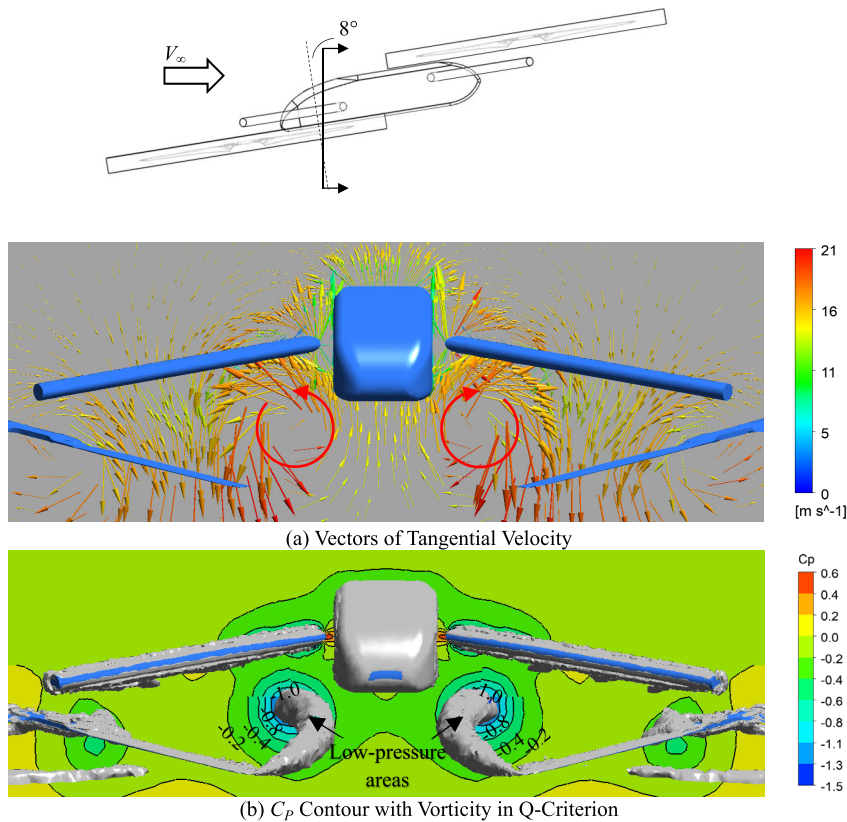
(a) Vectors of Tangential Velocity

(b) C_P Contour with Vorticity in Q-Criterion

FIGURE 9. Tangential velocity and C_P distribution highlighting the tip vortices of front rotors.

To find the cause of the trough at Point D, three cases at φ_f values of 128°, 146° (Point D) and 167° are inspected. the C_P contours at C-C section crossing the front arms are examined as shown in Fig. 14. Rotor turns to a parallel position beneath the front arms at Point D ($\varphi_f = 146°$). The pressure decreases on the bottom of front arms as the result of the low-pressure area of the front rotors, reducing C_L. It is noted that the impact of negative-pressure imposed on the front arms at Point D is larger than that of the high-pressure on rear arms at point C, supporting the higher amplitude of trough D than that of C.

To summarize, the variation of ΔC_L are determined by the azimuth angles of rotor blades. The sine-like variation law of ΔC_L is induced by the low-pressure over the upper surface of the front rotors as the rotor rotates. This flow mechanism of change pressure is responsible for the change of lift of body and arms. Abrupt changes only occur when the rotor sweeps over the arms. This impact of front rotors is larger than that of the rear ones. Due to the different rotational speeds between the front and rear rotors, the interval between the two dives also changes periodically. The physical representations of discussed interest points are listed in TABLE 8.
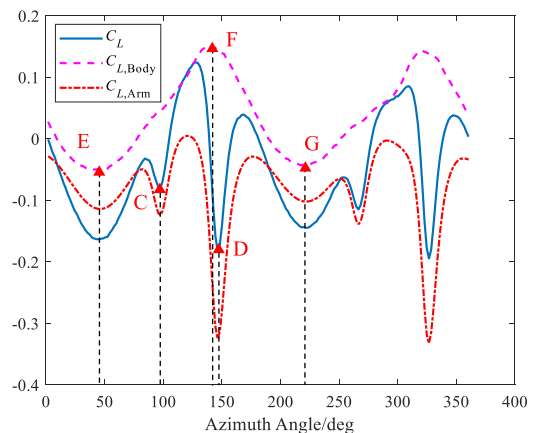

FIGURE 10. Decomposition of C_L for body and arms (C corresponds to $\varphi_f = 98°$, D corresponds to $\varphi_f = 146°$, E corresponds to $\varphi_f = 43°$, F corresponds to $\varphi_f = 139°$, G corresponds to $\varphi_f = 222°$, where the front rotor rotates by about 180° from Point E.)

B. VARIATION IN DRAG COEFFICIENT

This part discusses aerodynamic interference effects of changing fuselage drag. The analysis applies the same method used in part A, and time-domain analysis is performed to study the change of fuselage drag due to the
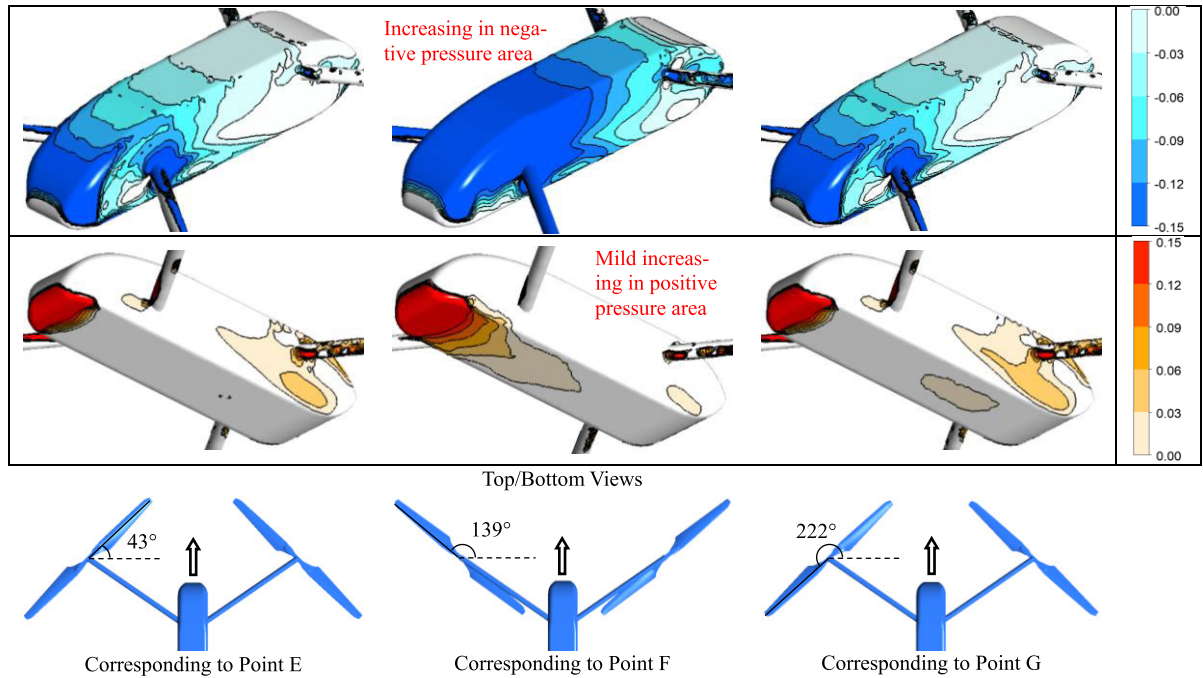
Top/Bottom Views

Corresponding to Point E Corresponding to Point F Corresponding to Point G

FIGURE 11. ΔC_P distribution over the body due to rotor rotation results in lift increasing (Point E, F, and G).

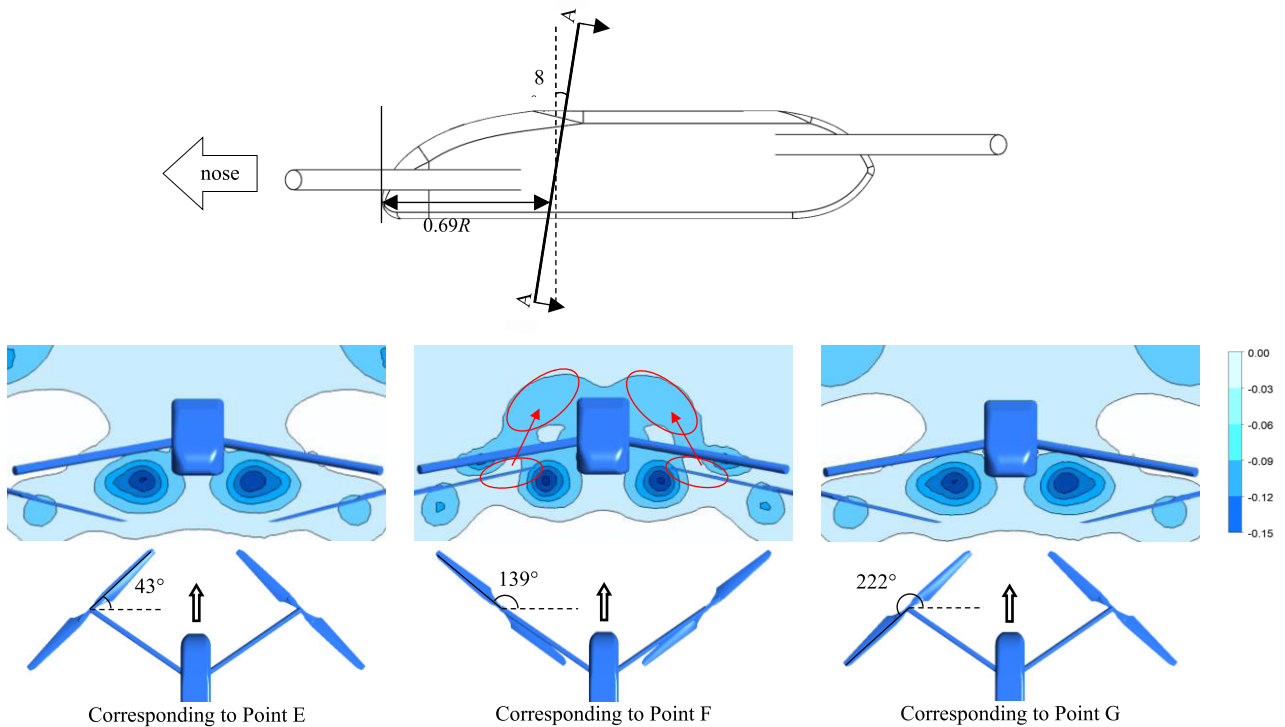Corresponding to Point E Corresponding to Point F Corresponding to Point G

FIGURE 12. ΔC_P for the A-A plane (E-G interval).

rotor rotation. The results in Fig. 15 shows the curves of C_D for a random cycle (one revolution) of the front rotors, with the same time interval as ΔC_L in Fig. 8.

The drag of fuselage (C_D) is decomposed into the contribution of arms and that of body, as shown in Fig. 15. Results indicate that the drag is mainly contributed by component
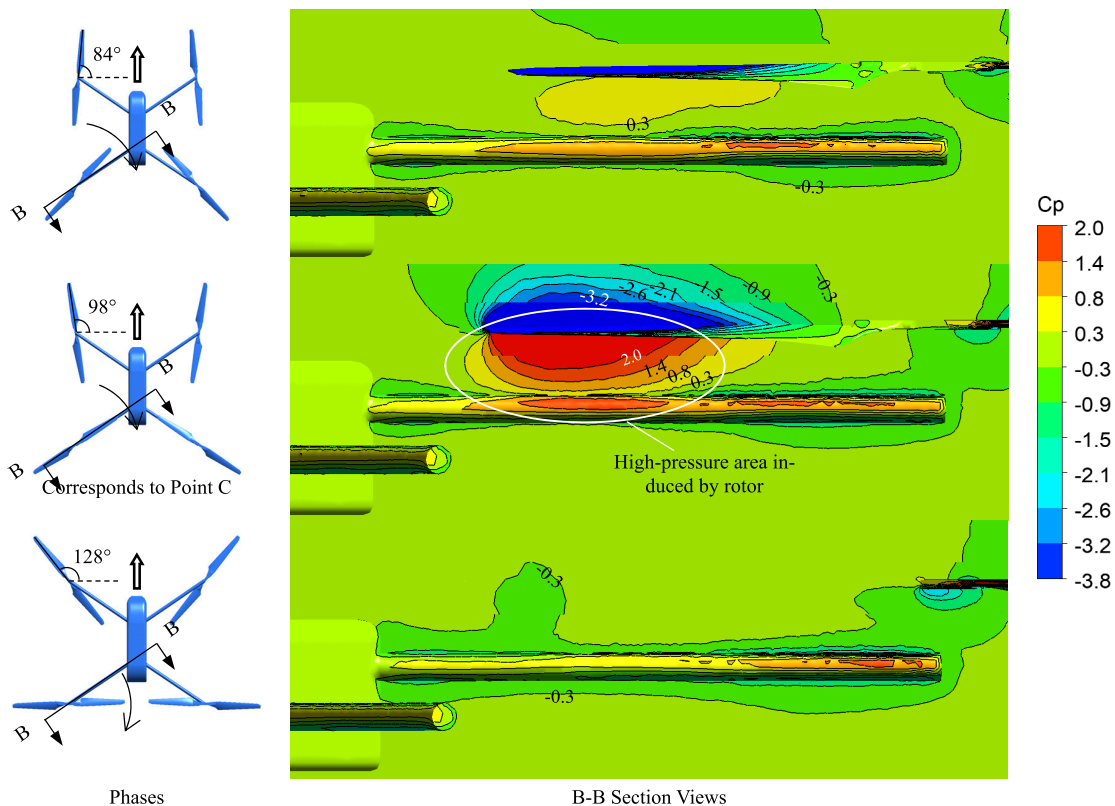
FIGURE 13. High pressure region of the rotor blade sweeps over the rear arm increasing the local pressure (the figure in the middle corresponds to Point C).
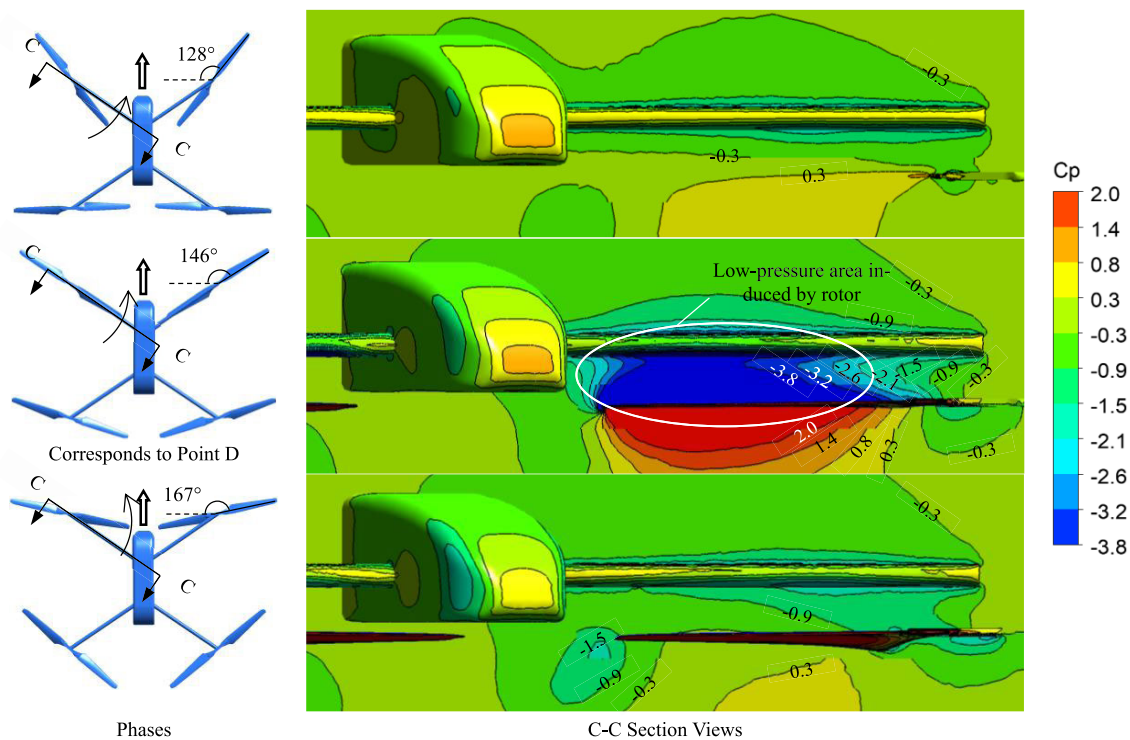

FIGURE 14. Low pressure region of the rotor blade sweeps through the front arm reducing the local pressure (the figure in the middle corresponds to Point D).

TABLE 8. Interpretations of interest points in ΔC_L.

Interest Point	Physical representation	Phase Angle (φ_f)
C	The rear rotor blade sweeps over the rear arm.	98°
D	The front rotor blade sweeps through the front arm.	146°
E	The upwash reaches to the minimum for the first time.	43°
F	The upwash reaches to the maximum for the first time.	139°
G	The upwash reaches to the minimum for the second time.	222°

TABLE 9. Interpretations of interest points in ΔC_D.

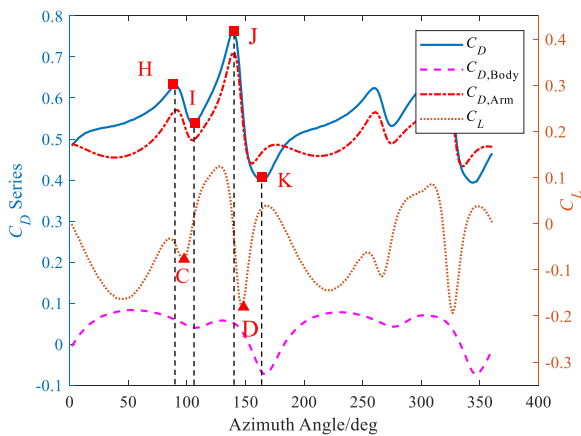| Interest Point	Physical Representation	Phase Angle (φ_f)
H		90°
I	The rear rotor blade passes through the rear arm.	105°
J		139°
K	The front rotor blade passes through the front arm.	165°

FIGURE 15. Decomposition of C_D for body and arms contrasting with C_L (ΔC_D-related interest points are marked with squares).

of arms rather than that of the body. This is an accordance with the ratio of (projection) area of arms over that of body being 2.19 (S_{Arm} / S_{Body} = 2.19). This plot shows that variation of drag tends to repeats at a period of 180 degrees, implying that the aerodynamic interference is dominated by the motion of a single blade. For further discussion, interest points are marked at the peaks (H, J) and troughs (I, K) of the curve.

To study the flow mechanisms associated with the variations of drag due to rotor rotation, pressure distribution around the arms at the section plane D-D is examined, as shown in Fig. 16. Point H ($\varphi_f = 90°$) and I ($\varphi_f = 105°$) highlight the impacts of the high-pressure region beneath the rear rotor blade. The motion of rear rotor blades alters the local pressure distribution of rear arms: the approaching blade tends to increase the high pressure on the upwind side of the arms thereby increase drag; when blade passing through the rear arms at Point I, the rotor-induced high pressure shifts from the upwind side to the downwind side of the arm, causing a rapid drop of drag; the departing blade gradually decrease the high pressure from the downwind

side of the arms, drag gradually get recovered (increased), as shown in Fig. 16a and b. in a similar manner, Point J ($\varphi_f = 139°$) and K ($\varphi_f = 165°$) highlight the impacts of the low-pressure region above the front rotor blade. As front rotor blades passing through the front arms at Point J, the rotor-induced low pressure shifts from downwind side to the upwind of the arms, leading to the rapid increasing in drag. TABLE 9 lists the physical representations of these interest points.

C. VARIATION IN PITCHING MOMENT COEFFICIENT

Pitching moment of fuselage is an important aerodynamic parameter to be considered in the control system of quadcopter. This part discusses the flow mechanism of aerodynamic interference changing the moment of the fuselage. The variation of moment for a cycle is presented in Fig. 17. The positive value for the average pitching moment increment denotes the tendency of nose-up due to the rotor rotation. To investigate the reason for that, ΔC_P at $\varphi_f = 128°$ is evaluated according to (4). The change of pressure on x-z plane is shown as the contours in Fig. 18. This figure shows that ΔC_P on the top fuselage is lower than that on the bottom part, and the lowest ΔC_P can be found in the vicinity of the nose. Around the nose part, ΔC_P is negative on the upper surface, and positive on the lower surface, contributing a positive lift on the nose part. In the aft part of fuselage, ΔC_P is distributed in an upside-down pattern of the distribution around the nose, this contributes to a negative lift on the aft part. As a result, ΔC_P distribution on nose and aft parts leads to upward pitching moments of the fuselage.

The curves of ΔC_L and ΔC_M in Fig. 17 are plotted with the same x-axis, showing that the variation of moment (ΔC_M) is in accordance with the change of lift. This indicates that the deviation of ΔC_M might be associated with the same flow mechanism discussed in the variation of lift. The pitching moment (C_M) is further decomposed into the contributions of body and arm. As shown in Fig. 19. At Point C and D, rotor blades induce high-pressure areas above rear arms and low-pressure areas under the front arms, as elaborated in part A. These are mainly responsible for the abrupt changes of $C_{M,\text{Arm}}$.
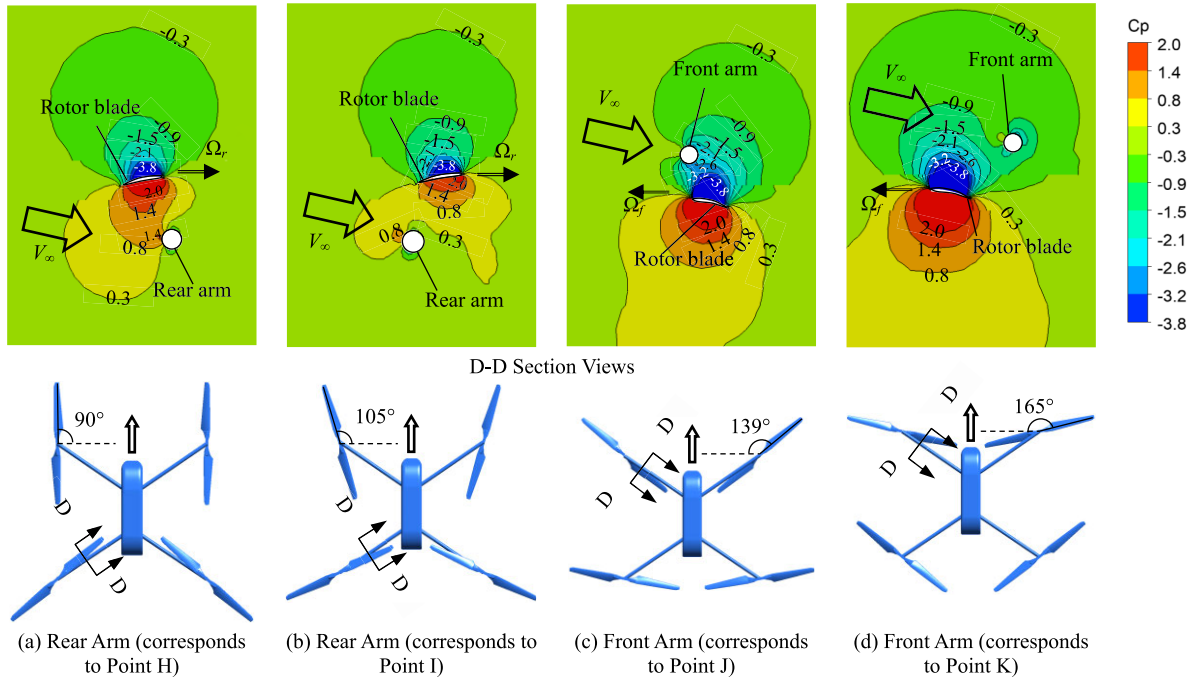
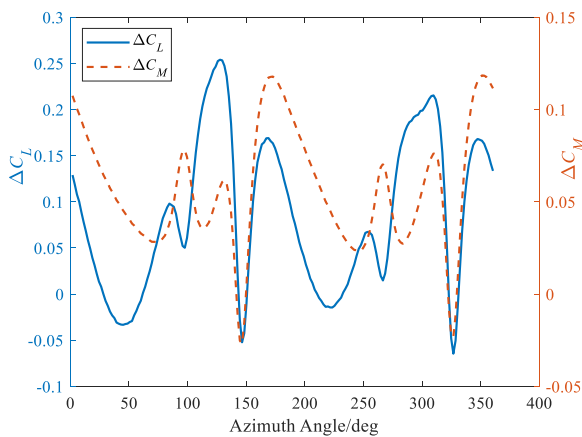**FIGURE 16.** ΔC_P distribution over arms (D-D section) as rotor blades passing through.

FIGURE 17. Comparison between ΔC_L and ΔC_M.

It is noted that the moment imposed on the body $C_{M,\mathrm{Body}}$ exhibits sine-like variation. Fig. 20 compares the curves of $C_{L,\mathrm{Body}}$ with that of and $C_{M,\mathrm{Body}}$. Interest points are marked for the following discussing of flow mechanisms. The $C_{L,\mathrm{Body}}$ curve keeps rising in the T-U interval, while the $C_{M,\mathrm{Body}}$ curve keeps a same trend in the V-W interval. Nevertheless, $C_{L,\mathrm{Body}}$ changes in an opposite direction of $C_{M,\mathrm{Body}}$ in the T-V interval and the same is true in the U-W interval. To find out the reasons, the change of pressure over the body surface is evaluated in these interest points, namely V, T, W and U. Metrics are defined in (5) and (6) where the superscripts represent these interest points and the difference between two interest points.

$$\Delta C_P^{\mathrm{V-T}} = C_P^{\mathrm{V}} - C_P^{\mathrm{T}} \tag{5}$$

$$\Delta C_P^{\mathrm{W-U}} = C_P^{\mathrm{W}} - C_P^{\mathrm{U}} \tag{6}$$

Fig. 21 illustrates the $\Delta C_P^{\mathrm{V-T}}$ and $\Delta C_P^{\mathrm{W-U}}$ contours over the top and bottom surface of body. Figures one the left shows that pressure decreases on the upper surface and increases on the lower surface in T-V interval, contributing to the rising of $C_{L,\mathrm{Body}}$ curve in Fig. 20. The pressure variation on the nose part of the bottom-body (marked with a red circle) leads to a nose-down moment, while the C_P variation on the top-body has small impact on pitching moment due to its pressure center close to the center of gravity (c.g.). Two figures on the right depicts the pressure change in U-W interval. Pressure decreases on both side of the body, with the relatively large area on the bottom-body. This leads to a decrease in lift, corresponding to the drop of $C_{L,\mathrm{Body}}$ curve in U-W interval. As for pitching moment concerned, the distribution of ΔC_P on the top-body exhibits decreases on the nose part and increase on the aft part, tends to cause a nose-up moment. In short, the opposite change of $C_{L,\mathrm{Body}}$ and $C_{M,\mathrm{Body}}$ in T-V and U-W intervals is evidenced by the distribution of pressure variation.

To investigate the cause of different change in pressure between T-V and U-W intervals, the flow field close to the nose part of body is analyzed. Fig. 22 shows the C_P contours on E-E plane at the interest points of T and V. the two low-pressure centers in the red square represent the cores of the tip vortex leaving from the front rotor blades. These vortex cores locates beneath the body. It is noted that the blades of front rotors turn away from the nose part from T to V, leaving weak vortex cores at E-E plane. The lower intensity in the low pressure of vortex cores means the negative
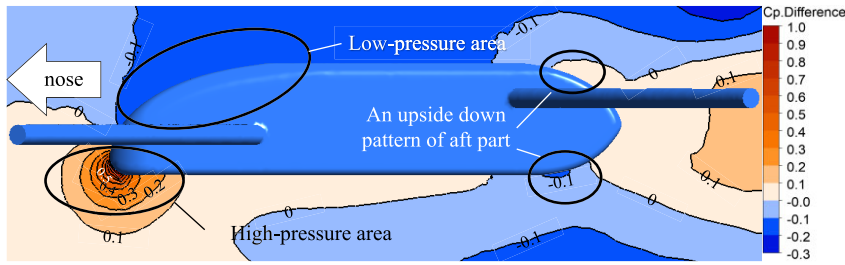
FIGURE 18. ΔC_P contour at $\varphi_f = 128°$ (the change in pressure distribution over the body, causing an upward pitching moment).
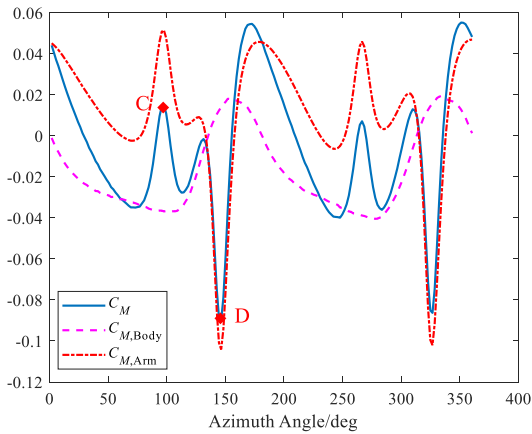

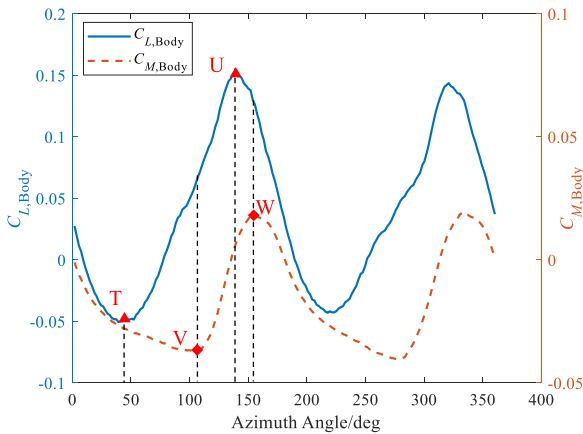
FIGURE 19. Decomposition of C_M for body and arms.

FIGURE 20. Correlation between $C_{L,\text{Body}}$ and $C_{M,\text{Body}}$ of quadcopter (T corresponds to $\varphi_f = 43°$, U corresponds to $\varphi_f = 139°$, V corresponds to $\varphi_f = 107°$, W corresponds to $\varphi_f = 156°$).

values of $\Delta C_P^{\text{V}-\text{T}}$. These weak vortex cores of front rotor blades is responsible for the pressure decrease on the nose part of the bottom-body (mark in the red cycle of Fig. 21), causing the opposite change of $C_{L,\text{Body}}$ and $C_{M,\text{Body}}$ in T-V interval.

Aerodynamic interference in U-W interval is investigated in a same approach. Fig. 23 shows the C_P contours on E-E plane at the interest points of U and W. It is noted that the rotor blades pass through E-E plane in U-W interval, directly changing the pressure around the nose part of the body. The

low-pressure region over the upper surface of rotor blades leads to the significant decrease of pressure on the left, right and top sides of body nose. Because the bottom-body is close to the plane of rotor disc, the impact of low-pressure region above the upper blade surface tends to be eliminated by the high pressure beneath the lower blade surface, leading to a mild pressure decreases on the lower surface of body's nose part. In short, the pressure induced by blade surface is mainly responsible for the different pressure variation between top and bottom surface of body nose (right figures in Fig. 21), as well as the opposite change of $C_{L,\text{Body}}$ and $C_{M,\text{Body}}$ in U-W interval.

To study the impacts of blade tip vortex on the body surface, A survey plane is selected where tip vortex passing through, as shown in the top of Fig. 24. The vortex flux crossing a survey plane is evaluated by (7).

$$\text{Vortex Flux} = \int 2\omega \mathrm{d}S \qquad (7)$$

The quantity of vortex flux crossing survey plane and the coefficient of lift is plotted in Fig. 24. This plot shows that the change of vortex flux keeps a same trend with that of $C_{L,\text{Body}}$. It increases in the T-V interval and decreases in the U-W interval, as presented in Fig. 21. It is noted that the variation of vortex flux coincides with the change of the body lift, implying their causal relationship. In terms of flow physics, the vortex flux causes the wash up flow highlighted by its tangential velocity shown in Fig. 9. This wash up leads to the pressure decreasing on the top-body and pressure increasing on the bottom-body, therefore changes the lift and moment of the body.

To investigate the cause of abovementioned vortex flux variation, tip vortexes of rotor blades are visualized in Fig. 25. Definitions of blade and tip vortex are made in Fig. 25a for following discussions. Vortex 1 is detached from the tip of blade 1 and vortex 2 is for blade 2. Fig. 25b highlights the tip vortex with the vorticity in Q-Criterion and C_P contours on A-A plane. As the front rotor rotates from point T to point V, vortex 1 at A-A plane moves inward and merges with vortex 2 of which position at A-A plane keeps almost unchanged. Those phenomena increase the intensity of vortex flux and the upwash to the body.
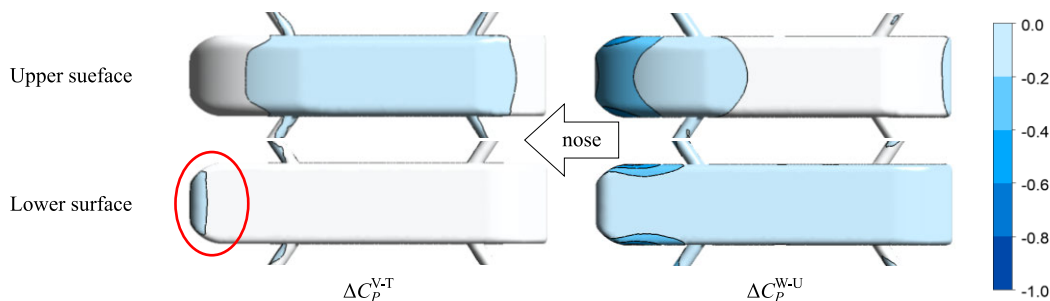
FIGURE 21. ΔC_P^{V-T} and ΔC_P^{W-U} contour on the top-body and bottom-body (the inhomogeneous distribution of pressure at nose and aft part makes the $C_{L,Body}$ and $C_{M,Body}$ curves out of sync).
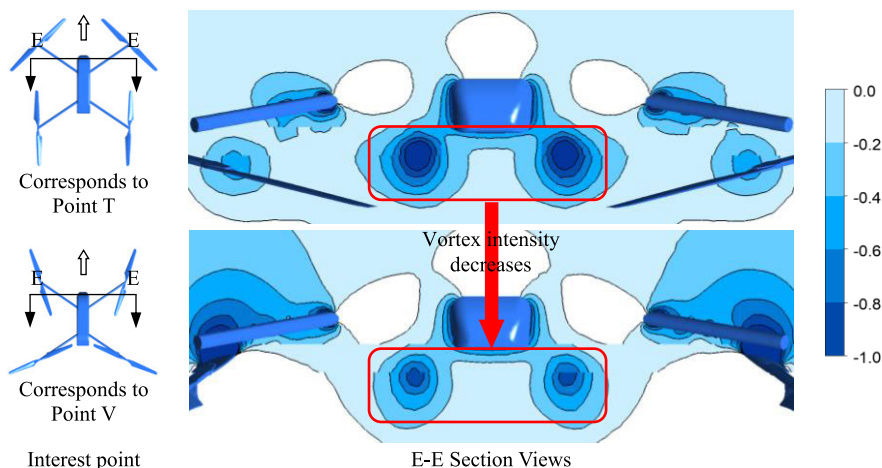

FIGURE 22. C_P contour at nose part from interest point T to V (vortex dissipation causes a weaker upwash, leading to the local lift loss).
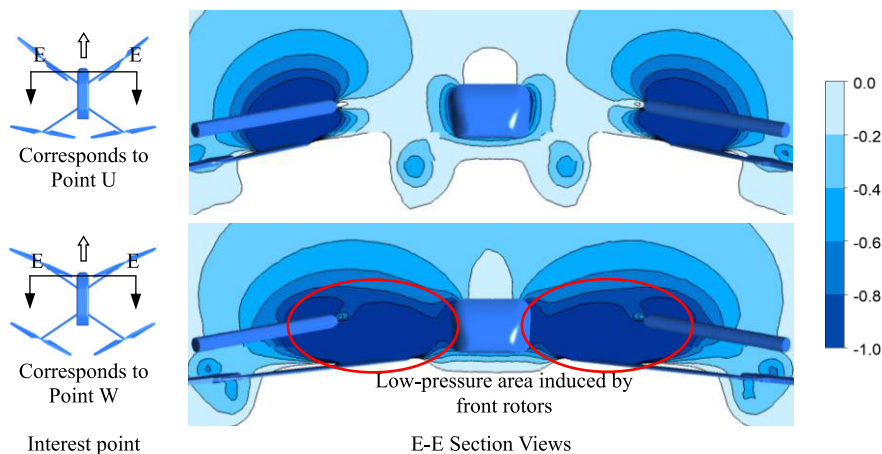

FIGURE 23. C_P contour at nose part from interest point U to W (the pressure change is straightly deduced by the front rotors).

In the U-W interval, the vortex flux decreases, corresponding to ΔC_P^{W-U} shown in Fig. 24b. As shown in Fig. 26, without significant change of vortex location, the decreases of vortex flux might be attributed to viscous dissipation which reduces its intensity as it flows downstream. The attenuated

vortex intensity tends leads to the pressure increasing on the top-body and decreasing on the bottom-body.

TABLE 10 lists the physical representation of interest points marked in Fig. 7. To summarize, the variations of ΔC_M are associated with that of ΔC_L. Aerodynamic interference
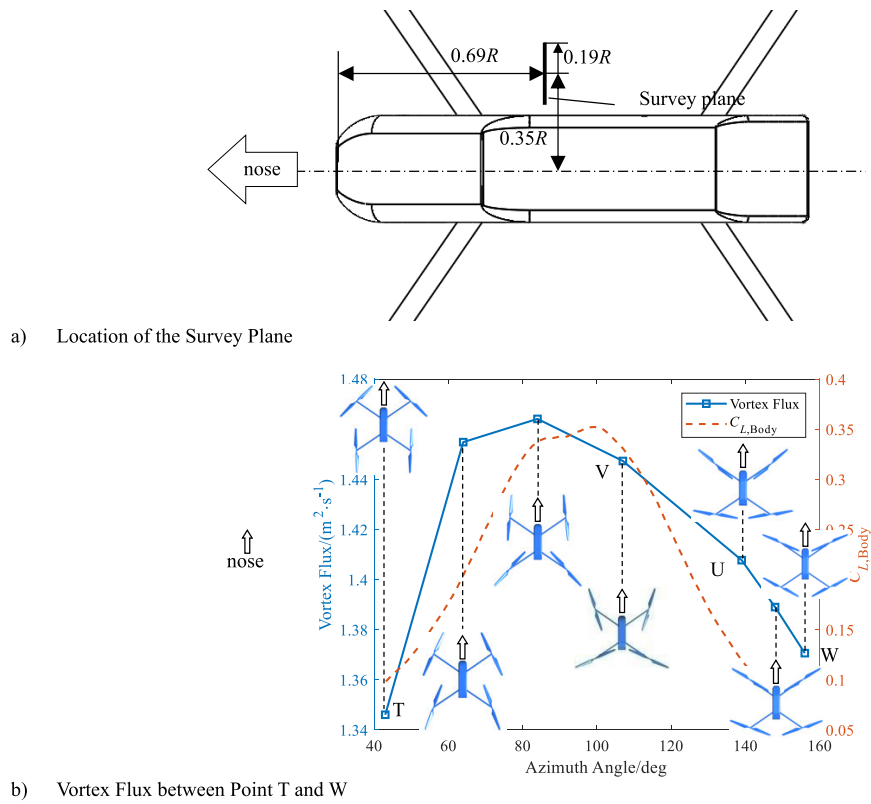
a)   Location of the Survey Plane

b)   Vortex Flux between Point T and W

FIGURE 24. Variation of vortex flux (absolute values) for the survey plane (interval T to W).

(a) Numbering of the Blade and Vortex
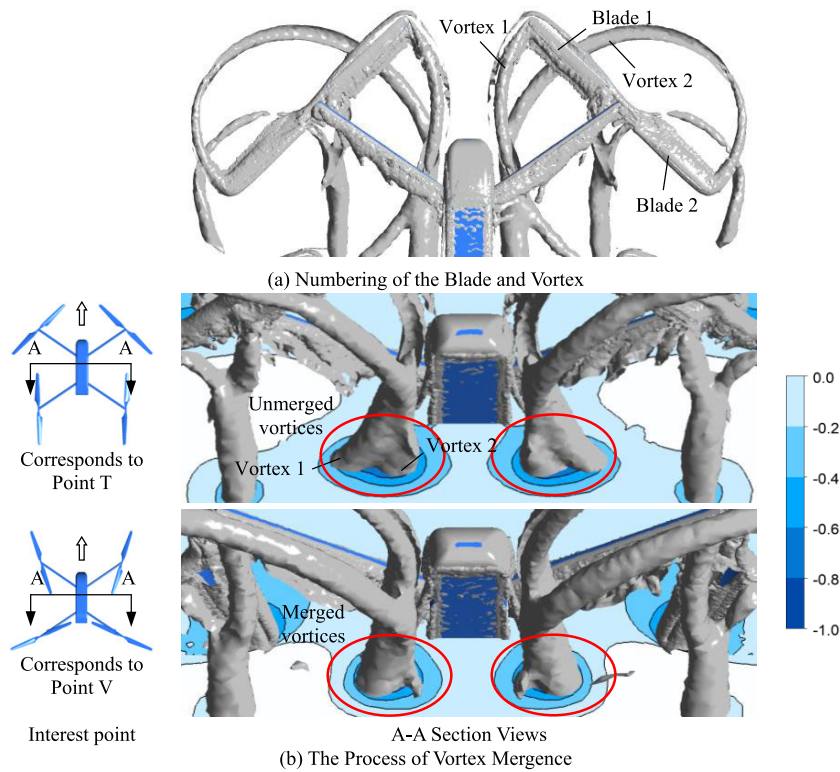

(b) The Process of Vortex Mergence

FIGURE 25. C_P contour and vorticity in Q-Criterion on A-A plane from interest point T to V (vortex 1 moves to the x-z plane and fuses with vortex 2, forming a stronger vortex).
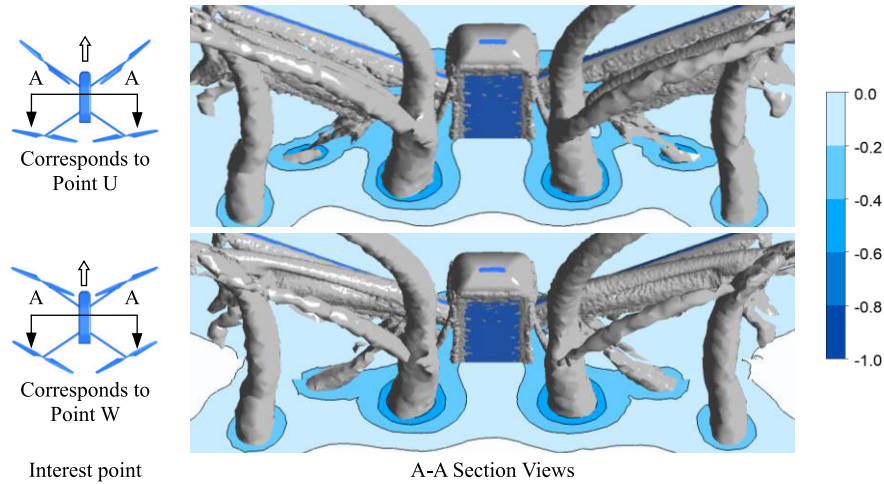
FIGURE 26. C_P contour and vorticity in Q-Criterion on A-A plane from interest point U to W.

TABLE 10. Interpretations of interest points in $C_{L,\text{Body}}$ and $C_{M,\text{Body}}$.

Interest Point	Status of Interest Point	Phase Angle (φ_f)
T	The first trough for $C_{L,\text{Body}}$	43°
U	The first peak for $C_{L,\text{Body}}$	139°
V	The first trough for $C_{M,\text{Body}}$	107°
W	The first peak for $C_{M,\text{Body}}$	156°

due to the rotor rotation contributes to an upward pitching moment on average. Merging and moving downstream of the tip vortices are associated with the change of the lift and pitching moment of body, as evidenced by the variation of tip vortex intensity and corresponding wash up at survey plane. Rotor blades passing through the arms is responsible for the abrupt change in aerodynamic force imposed on the arms.

IV. CONCLUSION

This paper elaborates the aerodynamic interference of rotor imposed on the fuselage of quadcopter by using CFD simulations. Frequency-domain and time-domain analysis are performed to study aerodynamic forces and moment. The effect of rotor-fuselage aerodynamic interference and flow mechanisms are investigated. Conclusions are given as follows.

ΔC_L, ΔC_D and ΔC_M are caused by the rotation of rotors with positive average values. Compared with the isolated fuselage, the aerodynamic interference due to rotor rotations

accounts for about 67% additional lift, 13% additional drag, and 90% pitching up moment under a typical cruise flight condition.

The sine-like periodical variation in aerodynamic forces and moment of fuselage is caused by the pressure distribution changes due to the rotation of rotor blades. The variation of ΔC_L is mainly generated by the low-pressure area on the top-body. The area in the vicinity of nose part affected by upwash is larger than that of the aft part for the existence of the extreme-pressure area, leading to the nose up pitching moment.

Periodical abrupt changes of aerodynamic forces are associated with the motion of rotors blades passing through the arms. Pressure distribution on the arms is affected by the low-pressure and high-pressure areas over blade surfaces, leading to the periodical changes of the lift, drag and pitching moment at certain azimuth angles where rotors passing through the arms.

Efforts are made in this work to investigate the transient effects of aerodynamic interference imposed on the fuselage of quadcopter. However, there are a few aspects can be improved: simulations are limited to the forward flight condition, additional lateral aerodynamic forces might not be negligible under sideslip condition and should be considered; This work assumes rigid fuselage and rotor blades and this might be unsuitable for large-scale quadcopter. This could be improved by involving aero elasticity analysis in future works.

REFERENCES

[1] C. Powers, D. Mellinger, A. Kushleyev, B. Kothmann, and V. Kumar, "Influence of aerodynamics and proximity effects in quadrotor flight," in *Proc. 13th Int. Symp. Experim. Robot.* Berlin, Germany: Springer, 2013, pp. 289–302, doi: 10.1007/978-3-319-00065-7_21.

[2] N. Michael, D. Mellinger, Q. Lindsey, and V. Kumar, "The GRASP multiple micro-UAV testbed," *IEEE Robot. Autom. Mag.*, vol. 17, no. 3, pp. 56–65, Sep. 2010, doi: 10.1109/MRA.2010.937855.

[3] A. Kushleyev, D. Mellinger, C. Powers, and V. Kumar, "Towards a swarm of agile micro quadrotors," *Auton. Robots*, vol. 35, no. 4, pp. 287–300, 2013, doi: 10.1007/s10514-013-9349-9.

[4] M. W. McConley, M. D. Piedmonte, B. D. Appleby, E. Frazzoli, E. Feron, and M. A. Dahleh, "Hybrid control for aggressive maneuvering of autonomous aerial vehicles," in *Proc. 19th DASC. Digit. Avionics Syst. Conf.*, Oct. 2000, pp. 1E4/1–1E4/8 , doi: 10.1109/DASC.2000.886897.

[5] P.-J. Bristeau, P. Martin, E. Salaun, and N. Petit, "The role of propeller aerodynamics in the model of a quadrotor UAV," in *Proc. Eur. Control Conf. (ECC)*, Aug. 2009, pp. 683–688, doi: 10.23919/ECC.2009.7074482.

[6] M. S. Alvissalim, B. Zaman, Z. A. Hafizh, M. A. Ma'sum, G. Jati, W. Jatmiko, and P. Mursanto, "Swarm quadrotor robots for telecommunication network coverage area expansion in disaster area," in *Proc. SICE Annu. Conf. (SICE)*, Aug. 2012, pp. 2256–2261.

[7] H. D. Nguyen, L. Yu, and K. Mori, "Aerodynamic characteristics of quadrotor helicopter," in *Proc. AIAA Flight Test. Conf.*, Jun. 2017, p. 3141, doi: 10.2514/6.2017-3141.

[8] J. Y. Hwang, M. K. Jung, and O. J. Kwon, "Numerical study of aerodynamic performance of a multirotor unmanned-aerial-vehicle configuration," *J. Aircr.*, vol. 52, no. 3, pp. 839–846, May 2015, doi: 10.2514/1.C032828.

[9] D. Barcelos, A. Kolaei, and G. Bramesfeld, "Aerodynamic interactions of quadrotor configurations," *J. Aircr.*, vol. 57, no. 6, pp. 1074–1090, 2020, doi: 10.2514/1.C035614.

[10] J. Luo, L. Zhu, and G. Yan, "Novel quadrotor forward-flight model based on wake interference," *AIAA J.*, vol. 53, no. 12, pp. 3522–3533, Dec. 2015, doi: 10.2514/1.J053011.

[11] J. G. Leishman, "Momentum analysis in forward flight," in *Principles of Helicopter Aerodynamics*. New York, NY, USA: Cambridge Univ. Press, 2006, p. 94.

[12] W. Fu, J. Li, and H. Wang, "Numerical simulation of propeller slipstream effect on a propeller-driven unmanned aerial vehicle," *Proc. Eng.*, vol. 31, pp. 150–155, Jan. 2012, doi: 10.1016/j.proeng.2012.01.1005.

[13] M. Misiorowski, F. Gandhi, and A. A. Oberai, "Computational study on rotor interactional effects for a quadcopter in edgewise flight," *AIAA J.*, vol. 57, no. 12, pp. 5309–5319, Dec. 2019, doi: 10.2514/1.J058369.

[14] D. P. Witkowski, A. K. H. Lee, and J. P. Sullivan, "Aerodynamic interaction between propellers and wings," *J. Aircr.*, vol. 26, no. 9, pp. 829–836, Sep. 1989, doi: 10.2514/3.45848.

[15] D. Kaya and A. T. Kutay, "Aerodynamic modeling and parameter estimation of a quadrotor helicopter," in *Proc. AIAA Atmos. Flight Mech. Conf.*, Jun. 2014, p. 2558, doi: 10.2514/6.2014-2558.

[16] Y. M. Park and O. J. Kwon, "Simulation of unsteady rotor flow field using unstructured adaptive sliding meshes," *J. Amer. Helicopter Soc.*, vol. 49, no. 4, pp. 391–400, 2004.

[17] C. Allen, "Parallel flow-solver and mesh motion scheme for forward flight rotor simulation," in *Proc. 24th AIAA Appl. Aerodyn. Conf.*, Jun. 2006, p. 3476, doi: 10.2514/6.2006-3476.

[18] M. Misiorowski, F. Gandhi, and P. Anusonti-Inthra, "Computational analysis of rotor-blown-wing for electric rotorcraft applications," *AIAA J.*, vol. 58, no. 7, pp. 2921–2932, Jul. 2020, doi: 10.2514/1.J058851.

[19] R. Niemiec and F. Gandhi, "Effect of elastic blade deformation on trim and vibratory loads of a quadcopter," in *Proc. 73rd Annu. Forum Amer. Helicopter Soc., AHS Paper*, 2017, pp. 2017–2073.

• • •